

7. Hierarchical modeling examples

The objective of this chapter is to apply the hierarchical modeling approach discussed in Chapter 1 to three selected problems using the mathematical models studied in Chapters 3 and 4, and the finite element procedures introduced in Chapter 6. Therefore, it is a synthesis chapter in which the concepts and tools discussed so far are used to perform the finite element modeling of engineering structures.

The chosen examples are relatively simple, but rich enough to highlight several modeling issues. Indeed, the discussion will show the importance of hierarchical modeling and, depending on our experience regarding analyses, also contain some surprises. While we only consider three examples, it is important to recognize that the methodology used in the modeling and solutions is quite general.

7.1 Built-in cantilever subjected to a tip load

The physical problem we would like to study is summarized in Figure 7.1.

The aluminum plate/beam is connected to the steel plate by a process that guarantees that no relative displacements between the aluminum and steel plates occur at any point at the connecting section. The block is suspended by a thin cable which is pinned at the center of gravity of the rectangular end section. The total weight of the block plus the cable is given by P . We neglect the self-weight of the plates.

We are interested in predicting the displacements of the aluminum plate/beam and the stresses at sections $x = \ell/2$ (mid-span) and $x = 0$ (built-in end) for the relations $\ell/h = 100$, $\ell/h = 10$ and $\ell/h = 5$. In order to set some values, let $h = 0.1$ m and $b = 0.01$ m which is also the thickness of the steel plate. The load P is scaled such that the maximum normal stress at the built-in end predicted by the Bernoulli-Euler beam model is $0.9\tau_y$, where $\tau_y = 223$ MPa is the yield stress of the aluminum used.

The sequence of models used in the hierarchical process is:

- Model 1: Bernoulli-Euler beam model
- Model 2: Timoshenko beam model
- Model 3 to 6: Plane stress models

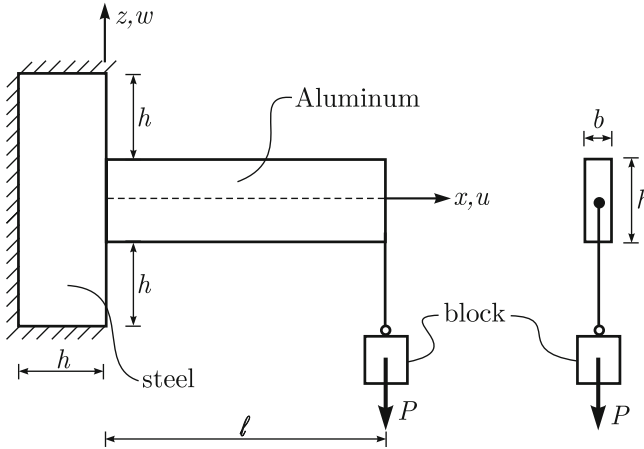


Fig. 7.1. Description of built-in cantilever. Material properties of the aluminum are $E = 70$ GPa, $\nu = 0.33$ and of the steel are $E = 210$ GPa, $\nu = 0.3$

We consider several plane stress models. However, their precise characterization is given as the modeling process unfolds.

7.1.1 Bernoulli-Euler beam model

The conditions that represent, in the context of the Bernoulli-Euler beam theory, the displacement restrictions and loading of the physical problem are summarized in Figure 7.2. Of course, in this model we are implicitly assuming that the steel plate is rigid.

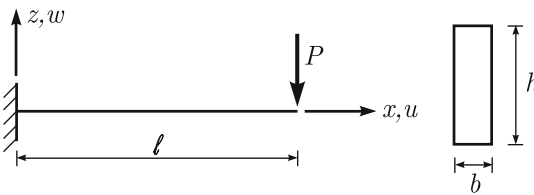


Fig. 7.2. Problem description for Bernoulli-Euler beam theory

These boundary conditions are

$$w(0) = 0, \quad \frac{dw}{dx}(0) = 0 \quad (7.1)$$

$$M(\ell) = 0, \quad V(\ell) = P. \quad (7.2)$$

The governing differential equation is

$$\frac{d^4 w}{dx^4} = 0 \quad (7.3)$$

since there is no distributed transverse load along the beam axis. The force boundary conditions described in (7.2) can be expressed in terms of the displacements by

$$M(\ell) = EI \frac{d^2 w}{dx^2}(\ell) = 0 \Rightarrow \frac{d^2 w}{dx^2}(\ell) = 0 \quad (7.4)$$

$$V(0) = EI \frac{d^3 w}{dx^3}(0) = P. \quad (7.5)$$

The integration of equation (7.3), considering the boundary conditions given in (7.1), (7.4) and (7.5) leads to the solution

$$w(x) = \frac{P}{6EI}(x^3 - 3\ell x^2). \quad (7.6)$$

Of course, from the above solution the moments and the shear forces can be obtained. The longitudinal displacement $u(x, z)$ can be directly derived from (7.6) considering the Bernoulli-Euler hypothesis that plane sections remain plane and orthogonal to the deformed beam axis. Therefore

$$u(x, z) = -z \frac{dw}{dx} = -\frac{Pz}{2EI}(x^2 - 2\ell x).$$

7.1.2 Timoshenko beam model

The characterization of the physical problem for the Timoshenko beam theory can also be described by Figure 7.2. Referring to the differential equations (4.238) and (4.239) which were derived in Section 4.2.8 and introducing $p = 0$ we obtain

$$-GA \left[\frac{d}{dx} \left(\frac{dw}{dx} - \beta \right) \right] = 0 \quad (7.7)$$

$$EI \frac{d^2 \beta}{dx^2} = -GA \left(\frac{dw}{dx} - \beta \right). \quad (7.8)$$

The boundary conditions are given by

$$\beta(0) = 0 \quad (7.9)$$

$$w(0) = 0 \quad (7.10)$$

$$M(\ell) = 0 \quad (7.11)$$

$$V(\ell) = P. \quad (7.12)$$

Taking the derivatives with respect to x in equation (7.8) and using (7.7), we arrive at

$$EI \frac{d^3 \beta}{dx^3} = 0$$

which can be integrated leading to

$$\beta(x) = C_2 \frac{x^2}{2} + C_1 x + C_0. \quad (7.13)$$

Considering equation (7.11) and that for the Timoshenko beam model $M = EI \frac{d\beta}{dx}$, we obtain

$$\frac{d\beta}{dx}(\ell) = 0. \quad (7.14)$$

Introducing (7.9) and (7.14) into (7.13), we obtain

$$\beta(x) = C_2 \frac{x^2}{2} - C_2 \ell x. \quad (7.15)$$

Recalling that for the Timoshenko model $V = -GA \left(\frac{dw}{dx} - \beta \right)$, the boundary condition (7.12), together with equation (7.8), gives

$$-GA \left(\frac{dw}{dx} - \beta \right) \Big|_{\ell} = P = EI \frac{d^2 \beta}{dx^2} \Big|_{\ell}.$$

Therefore from (7.15)

$$C_2 = \frac{P}{EI}$$

and

$$\beta(x) = \frac{P}{2EI} (x^2 - 2\ell x). \quad (7.16)$$

Introducing the above equation into (7.8)

$$\frac{dw}{dx} = \frac{P}{2EI} (x^2 - 2\ell x) - \frac{P}{GA}$$

which can be integrated to give

$$w(x) = \frac{P}{EI} \left(\frac{x^3}{6} - \frac{\ell x^2}{2} \right) - \frac{P}{GA} x + C.$$

Imposing the boundary condition (7.10), we obtain

$$w(x) = \frac{P}{6EI} (x^3 - 3\ell x^2) - \frac{P}{GA} x.$$

Introducing the shear correction factor for a rectangular cross-section (see discussion in Chapter 4) and using $A = bh$, we arrive at

$$w(x) = \frac{P}{6EI} (x^3 - 3\ell x^2) - \frac{12 + 11\nu}{10(1 + \nu)} \frac{P}{Gbh} x.$$

The longitudinal displacement $u(x, z)$ can be obtained considering that for the Timoshenko beam the sections remain plane and rotate by the angle $\beta(x)$. Therefore from (7.16)

$$u(x, z) = -z\beta = -\frac{Pz}{2EI} (x^2 - 2\ell x).$$

7.1.3 Plane stress solution

Consider the plane stress model of Figure 7.3 in which we also assume that the steel plate is rigid.

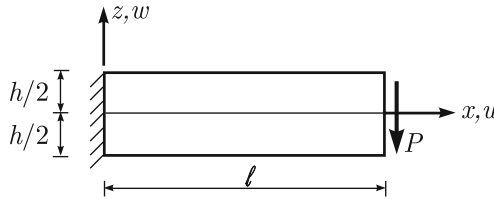


Fig. 7.3. Problem description in the context of the 2-D plane stress model

The displacement boundary conditions are

$$u(0, z) = 0 \tag{7.17}$$

$$w(0, z) = 0. \tag{7.18}$$

The force boundary conditions are given pointwise by

$$\mathbf{Tn} = \mathbf{f}^S$$

which for the free boundaries leads to

$$\tau_{zz}\left(x, \frac{h}{2}\right) = \tau_{zz}\left(x, -\frac{h}{2}\right) = 0$$

$$\tau_{xz}\left(x, \frac{h}{2}\right) = \tau_{xz}\left(x, -\frac{h}{2}\right) = 0.$$

For the edge defined by $x = \ell$, we have

$$\tau_{xx}(\ell, z) = f_x^S(\ell, z) = 0$$

$$\tau_{xz}(\ell, z) = f_z^S(\ell, z)$$

and $f_z^S(\ell, z)$ should represent the action of the load P . In other words, we need to distribute the load along a portion of the edge ($x = \ell$) denoted by L_P such that the resultant of the shear tractions (f_z^S) acting on L_P is equal to P , *i.e.*,

$$\int_{L_P} -f_z^S(\ell, z)b \, dL = P.$$

The choice of L_P and the functional distribution of f_z^S over L_P is actually a modeling consideration and depends on how the loading P is actually applied in the physical situation.

Since to impose the displacement boundary conditions given in equations (7.17) and (7.18) and to find an analytical solution for this problem is not an easy task, we seek instead the solution of the problem described in Figure 7.4.

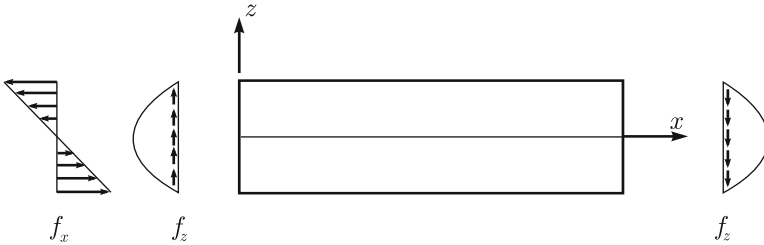


Fig. 7.4. Simplified 2-D plane stress problem, $L_P = h$

To relate the problems described in Figures 7.3 and 7.4 we need to impose at the edge $x = \ell$

$$\int_{-\frac{h}{2}}^{\frac{h}{2}} f_z^S(\ell, z)b \, dz = -P \quad (7.19)$$

and at the edge $x = 0$

$$\int_{-\frac{h}{2}}^{\frac{h}{2}} f_z^S(0, z)b \, dz = P \quad (7.20)$$

$$\int_{-\frac{h}{2}}^{\frac{h}{2}} f_x(0, z)zb \, dz = P\ell. \quad (7.21)$$

Of course, equation (7.20) guarantees the equilibrium in the vertical direction and equation (7.21) enforces global moment equilibrium. We choose the functional form of the traction distribution based on the shear stress distribution in beam models as previously discussed.

The derivations given below were reported in many textbooks and are repeated here merely for the convenience of the reader. We follow the classical textbook of Timoshenko and Goodier, 1970.

To derive the solution, we assume that the stress distributions are the same as that for a beam in bending. Hence

$$\tau_{xx}(x, z) = \frac{P(\ell - x)}{I}z = \frac{P(\ell - x)}{\frac{bh^3}{12}}z = \frac{12P(\ell - x)}{bh^3}z \quad (7.22)$$

$$\tau_{xz}(x, z) = -\frac{3P}{2bh} \left(1 - \frac{4z^2}{h^2}\right) = -\frac{P}{2I} \left(\frac{h^2}{4} - z^2\right) \quad (7.23)$$

$$\tau_{zz}(x, z) = 0.$$

This stress field satisfies all traction boundary conditions. Since there are no body forces, the differential equilibrium equations are (see equations (4.45) and (4.46))

$$\frac{\partial \tau_{xx}}{\partial x} + \frac{\partial \tau_{xz}}{\partial z} = 0$$

$$\frac{\partial \tau_{xz}}{\partial x} + \frac{\partial \tau_{zz}}{\partial z} = 0$$

which are satisfied by the stress field given in (7.22) and (7.23).

Using the appropriate constitutive equation (4.44) we obtain the strains

$$\varepsilon_{xx} = \frac{\sigma_{xx}}{E} = \frac{P(\ell - x)}{EI}z$$

$$\varepsilon_{zz} = -\frac{\nu}{E}\sigma_{xx} = \frac{-\nu P(\ell - x)}{EI}z$$

$$\gamma_{xz} = \frac{\tau_{xz}}{G} = -\frac{P}{2GI} \left(\frac{h^2}{4} - z^2\right).$$

The strain-displacement relations are imposed next and used to obtain, by integration, a single valued displacement field¹ that satisfies the displacement boundary conditions. Referring to equations (4.47) to (4.49), we write

$$\varepsilon_{xx} = \frac{\partial u}{\partial x} = \frac{P}{EI}(\ell - x)z$$

hence

¹ We note that not all stress fields that satisfy equilibrium generate, through the use of the constitutive equations, compatible strain fields, *i.e.*, strain fields which can be integrated to lead to a single valued displacement field, see Section 3.2.2. Therefore, methods of solution that use as primary variables the stresses, such as the Airy stress function method, must enforce, besides the equilibrium conditions, the strain compatibility relations written in terms of the stresses

$$u(x, z) = \frac{P}{EI}(\ell x - \frac{x^2}{2})z + f(z) \quad (7.24)$$

where $f(z)$ is a function of z only. Also

$$\begin{aligned} \varepsilon_{zz} &= \frac{\partial w}{\partial z} = \frac{-\nu P}{EI}(\ell - x)z \\ w(x, z) &= \frac{-\nu P}{EI}(\ell - x)\frac{z^2}{2} + g(x) \end{aligned} \quad (7.25)$$

where $g(x)$ is a function of x only. We also have

$$\gamma_{xz} = \frac{\partial u}{\partial z} + \frac{\partial w}{\partial x} = -\frac{P}{2GI} \left(\frac{h^2}{4} - z^2 \right). \quad (7.26)$$

Substituting equations (7.24) and (7.25) into equation (7.26), we obtain

$$\frac{P}{EI}(\ell x - \frac{x^2}{2}) + \frac{df(z)}{dz} + \frac{\nu P}{2EI}z^2 + \frac{dg(x)}{dx} = -\frac{P}{2GI} \left(\frac{h^2}{4} - z^2 \right). \quad (7.27)$$

Defining

$$G(x) = \frac{P}{EI}(\ell x - \frac{x^2}{2}) + \frac{dg(x)}{dx} \quad (7.28)$$

$$F(z) = \frac{\nu P}{2EI}z^2 - \frac{P}{2GI}z^2 + \frac{df(z)}{dz} \quad (7.29)$$

$$K = -\frac{Ph^2}{8GI}$$

we can re-write (7.27) as

$$G(x) + F(z) = K. \quad (7.30)$$

Since K is a constant and $G(x)$ and $F(z)$ are functions of x and z only, we conclude that $G(x)$ and $F(z)$ must be constant functions, *i.e.*,

$$G(x) = e$$

and

$$F(z) = d$$

where e and d are real constant values. Therefore (7.28) and (7.29) become

$$\begin{aligned} \frac{dg(x)}{dx} &= -\frac{P}{EI}(\ell x - \frac{x^2}{2}) + e \\ \frac{df(z)}{dz} &= -\frac{\nu P}{2EI}z^2 + \frac{P}{2GI}z^2 + d \end{aligned}$$

leading to

$$g(x) = -\frac{P}{EI}\left(\ell\frac{x^2}{2} - \frac{x^3}{6}\right) + ex + j \quad (7.31)$$

$$f(z) = -\frac{\nu P}{6EI}z^3 + \frac{P}{6GI}z^3 + dz + i \quad (7.32)$$

where j and i are also real constant values. Substituting (7.31) and (7.32) into (7.24) and (7.25) leads to

$$u(x, z) = -\frac{P}{2EI}(x^2 - 2\ell x)z - \frac{\nu}{6EI}Pz^3 + \frac{Pz^3}{6GI} + dz + i \quad (7.33)$$

$$w(x, z) = -\frac{\nu P}{2EI}(\ell - x)z^2 + \frac{P}{6EI}(x^3 - 3\ell x^2) + ex + j. \quad (7.34)$$

Since in the model of Figure 7.4 we are applying force boundary conditions along all boundaries, we need to suppress the rigid body motions while representing as close as possible the displacement boundary conditions for the problem of Figure 7.3. This condition allows us to determine the constants that appear in equations (7.33) and (7.34). We impose

$$u(0, 0) = 0$$

and

$$w(0, 0) = 0$$

that is, we fix the mid-point at the built-in end. These conditions lead to $i = j = 0$. However, the rotation about this point has still to be prevented and how to enforce this condition is not obvious. Referring to the problem of Figure 7.4, we choose to enforce

$$\frac{\partial u}{\partial z}(0, 0) = 0 \quad (7.35)$$

that is we impose that a vertical infinitesimal fiber with origin at the point $(0,0)$ remains vertical after the deformation has taken place. We note that other infinitesimal fibers along the edge $x = 0$ do not remain vertical, as detailed later. Another choice would be to impose $\frac{\partial w}{\partial x}(0, 0) = 0$, that is, to enforce that a horizontal infinitesimal fiber, at the built-in end, along the x axis, remains horizontal. Since the distortion $\gamma_{xz}(0, 0)$ is different from zero we can not satisfy both conditions simultaneously and, considering the physical problem, to prevent the rotation of the vertical fiber corresponds to an appropriate modeling assumption. We note that to fix the horizontal fiber corresponds to neglecting the effect on the transverse displacements of the distortion at point $(0, 0)$. Considering the boundary condition given in equation (7.35) and using equation (7.33), we obtain

$$\frac{\partial u}{\partial z}(0,0) = d = 0$$

and from (7.30) we obtain $e = -\frac{Ph^2}{8GI}$. Hence, the displacements are

$$u(x,z) = -\frac{P}{2EI}(x^2 - 2lx)z - \frac{\nu}{6EI}Pz^3 + \frac{Pz^3}{6GI} \quad (7.36)$$

$$w(x,z) = \frac{P}{6EI}(x^3 - 3lx^2) - \frac{\nu P}{2EI}(\ell - x)z^2 - \frac{Ph^2}{8GI}x. \quad (7.37)$$

Let us examine the longitudinal displacements at the built-in end, *i.e.*, $u(0,z)$. From equation (7.36)

$$u(0,z) = \frac{(2 + \nu)}{6EI}Pz^3 \quad (7.38)$$

and the shear strain at point $(0,0)$ can also be evaluated from equations (7.36) and (7.37)

$$\gamma_{xz}(0,0) = -\frac{Ph^2}{8GI}. \quad (7.39)$$

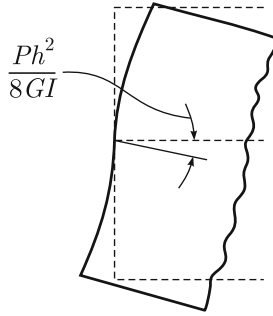


Fig. 7.5. Detail of the magnified displacements at built-in end

In Figure 7.5 we show the deformed and undeformed configurations at the built-in end for the data $E = 70$ GPa, $\nu = 0.33$, $P = 3345$ N, $h = 0.1$ m, $b = 0.01$ m magnified by a factor of 30. We note that the built-in end condition of the physical problem is not exactly satisfied as given by equations (7.17) and (7.18). We also show in Figure 7.5 the shear strain at the point $(0,0)$.

The natural choice for the next mathematical model in our sequence would be the 2-D plane stress model with the boundary conditions at the built-in end enforced exactly, *i.e.*, $u(0,z) = 0$ and $w(0,z) = 0$. However, there is no closed form analytical solution available under these conditions. Hence, we

Table 7.1. Displacement solutions for the first three models in the sequence

Model	u
Bernoulli-Euler	$-\frac{zP}{2EI}(x^2 - 2\ell x)$
Timoshenko	$-\frac{zP}{2EI}(x^2 - 2\ell x)$
Plane stress	$-\frac{zP}{2EI}(x^2 - 2\ell x) + \frac{Pz^3}{6EI}(2 + \nu)$

Model	w
Bernoulli-Euler	$\frac{P}{6EI}(x^3 - 3\ell x^2)$
Timoshenko	$\frac{P}{6EI}(x^3 - 3\ell x^2) - \frac{12+11\nu}{10(1+\nu)}\frac{P}{Gbh}x$
Plane stress	$\frac{P}{6EI}(x^3 - 3\ell x^2) - \frac{3}{2}\frac{P}{Gbh}x - \frac{\nu P}{2EI}(\ell - x)z^2$

take recourse to finite element modeling. Before doing so, let us obtain more insight into the problem by exploring the analytical solutions of the three first models of our sequence. We are interested in examining the difference in predictions both qualitatively and quantitatively of these models. In particular, we would like to see the effect on the predicted variables for different ratios between the length and height of the aluminum plate/beam.

In Table 7.1 we summarize the longitudinal and transverse displacement solution for the first three models in our sequence. We note that for the longitudinal displacement $u(x, z)$ both the Bernoulli-Euler and Timoshenko models give exactly the same predictions which correspond to a linear variation along the section height. This is, of course, linked to the kinematic hypothesis used in both models that plane sections remain plane. This linear variation is also predicted by the 2-D model which displays, in addition, a cubic term in z . At the built-in end, this is the only term which gives non-vanishing displacements and it is responsible for the violation of the boundary condition at this end as discussed earlier. In order to have an estimate of the magnitude of the displacement associated with this term when compared with the displacement predicted by the linear term, let us examine the displacement at the tip, *i.e.*, at $x = \ell$. We can write

$$u(\ell, z) = \frac{zP\ell^2}{2EI} \left(1 - \left(\frac{z}{\ell}\right)^2 \left(\frac{2 + \nu}{3}\right) \right)$$

which shows that the relative importance of the displacement associated with the cubic term with respect to the linear term is decreasing for increasing length to height ratios. In Table 7.2 we give some values for different length to height ratios. These reported values indicate that for usual beams ($10 \leq \ell/h \leq 100$) the contribution of the cubic term is very small.

Considering the transverse displacements, there is a common term to all models which corresponds to the effect of bending. For the Timoshenko and plane stress models, the second term represents the effect of shearing. We note that these shear terms are comparable since they are both linear with

Table 7.2. Displacement ratios for linear and cubic terms ($\nu = 0.33$)

ℓ/h	$u_{cubic}/u_{linear} (x = \ell, z = h/2)$
5	7.767×10^{-3}
10	1.942×10^{-3}
100	1.942×10^{-5}

respect to x and taking, for example, $\nu = 0.33$ the coefficients are $1.18 \frac{P}{Gbh}$ for the Timoshenko model and $1.5 \frac{P}{Gbh}$ for the plane stress model.

A quadratic variation of the transverse displacement through the beam height is predicted by the plane stress model which is linked to Poisson's ratio and corresponds to a zero contribution at points on the beam axis.

It is of interest to compare the relative importance of the bending and shear deformations for the resulting transverse displacements. Hence, we write the expressions for the transverse displacement of the axis as $\bar{w}(x)$ in a single expression for the three models

$$\bar{w}(x) = \frac{2P\ell^3}{Ebh^3} \left[\left(\frac{x}{\ell}\right)^3 - 3\left(\frac{x}{\ell}\right)^2 - k\left(\frac{h}{\ell}\right)^2 \left(\frac{x}{\ell}\right) \right] \quad (7.40)$$

where $k = 0$ for the Bernoulli-Euler model, $k = \frac{12+11\nu}{10(1+\nu)}$ for the Timoshenko model and $k = \frac{3(1+\nu)}{2}$ for the plane stress model. It is easy to see that the relative contribution of shear to the transverse displacement is proportional to the ratio $\left(\frac{h}{\ell}\right)^2$. Let us define

$$r_w = \left| \frac{\bar{w} - w_{BE}}{w_{BE}^{\max}} \right| \times 100 \quad (7.41)$$

which gives the percent of the transverse displacement due to shear measured and normalized with respect to the maximum displacement of the Bernoulli-Euler model. In expression (7.41) \bar{w} represents the total displacement of either the Timoshenko or the plane stress model and w_{BE} the transverse displacement of the Bernoulli-Euler model. Simplifying expression (7.41) yields

$$r_w = \frac{k}{2} \left(\frac{h}{\ell}\right)^2 \frac{x}{\ell} \times 100$$

which shows that the percent difference for a given point on the beam axis is proportional to the factor $\frac{k}{2} \left(\frac{h}{\ell}\right)^2$. Since k is independent of the ratio between the height and the length of the beam, the relative importance of shear deformations is given by the factor $\left(\frac{h}{\ell}\right)^2$. In Table 7.3, r_w is shown for $x = \ell$ (beam tip). We note, as expected, that the shear deformation contribution to the total transverse displacement is very small and that even for the relatively large ratio $h/\ell = 0.2$ the increase of transverse displacement is less than 4%.

Table 7.3. r_w for some ℓ/h ratios using $\nu = 0.33$

Model	$r_w(x = \ell)$		
	$\ell/h = 5$	$\ell/h = 10$	$\ell/h = 100$
Timoshenko	3.12600	0.78150	0.007815
Plane stress	3.99000	0.99750	0.009975

We recall that the stress distribution of the plane stress model is exactly that of the beam models since in the derivation of the plane stress solution we assumed from the onset that the stress distribution would be that given by the beam models (refer to equations (7.22) and (7.23)). Of course, the displacement solutions reported in Table 7.1 lead to these stresses through the compatibility and constitutive equations.

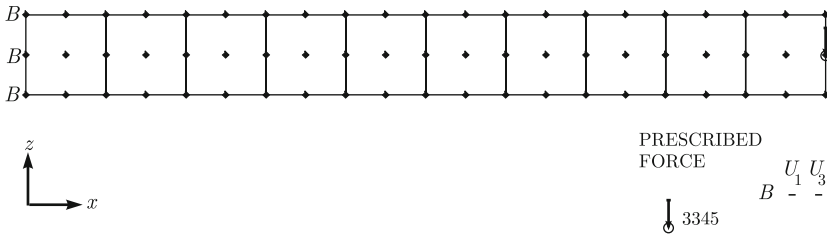


Fig. 7.6. Coarse finite element model (1×10), $\ell/h = 10$; $\nu = 0.33$

We return now to study the model described in Figure 7.3 and consider $\ell/h = 10$ and Poisson’s ratio $\nu = 0.33$. As mentioned before, we seek the solution of this model using finite elements. Since our objective is to discuss the solution of this mathematical model, we use a mesh refinement strategy to guarantee that our (final) finite element solution is “very” close to the solution of the mathematical model. We start with the model shown in Figure 7.6 in which we use ten 9-node displacement-based plane stress elements and refer to it as the 1×10 element model. We consider successive mesh refinements by subdividing each of the elements into four elements to obtain the 2×20 , 4×40 and 8×80 element models, and also give the results obtained using an extremely fine mesh of 64×640 elements. The last mesh results are really not needed but included to underline the convergence behavior. The 8×80 element model is shown in Figure 7.7.

In Figure 7.8, we report the strain energy values of the finite element solutions. We can clearly identify a convergent behavior since the absolute difference in predicted strain energy between two consecutive solutions is decreasing and eventually the difference is small (considering the two finest models).

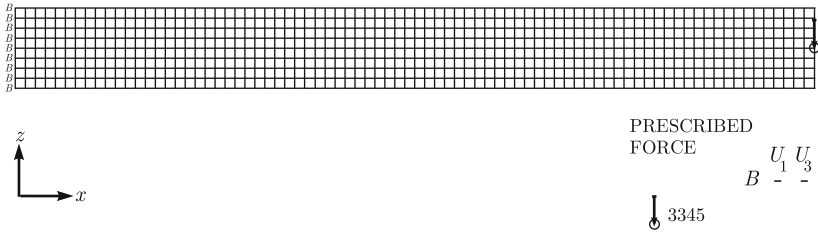


Fig. 7.7. (8×80) finite element model

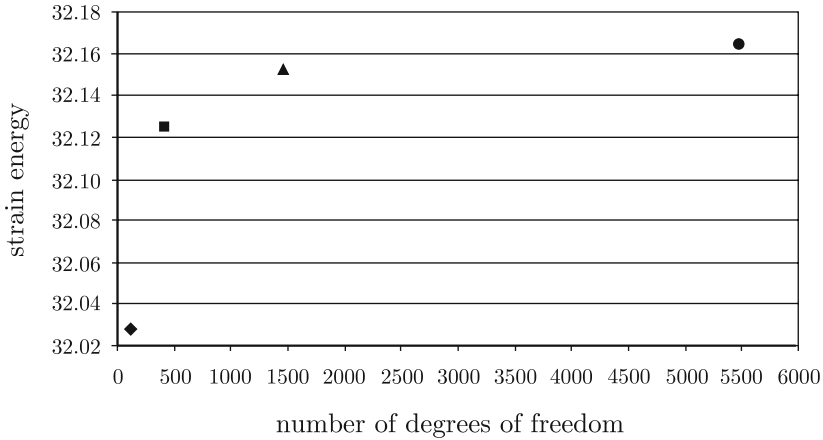


Fig. 7.8. Convergence in strain energy ($N.m$)

In Table 7.4, we report the predictions for the tip transverse displacement for all models. As expected, the convergent behavior of the finite element predictions is also observed. Note that the finite element solutions converge to a slightly smaller tip displacement value than given by the plane stress model studied earlier. The difference is quite small, but in the plane stress model studied analytically, the displacement boundary conditions do not represent exactly the built-in condition leading to a more flexible model.

In order to study the stress predictions, we select two sections: the built-in section and a section located at mid-span, *i.e.*, $x = \ell/2$. Let us first examine the predictions obtained with the 2×20 element model which already gives relatively accurate displacement predictions. The stress predictions² are shown in Figures 7.9 to 7.12. We note that the predictions for the mid-span section are reasonably close to those of the solution of models 1 to 3 (Model 1: Bernoulli-Euler beam model, see Section 7.1.1; Model 2: Timoshenko beam model, see Section 7.1.2; Model 3: Plane stress model, see Section 7.1.3).

² Here we also use the parabolic shear stress distribution for the Bernoulli and Timoshenko beam elements as the analytical solutions, see Sections 4.2.2 and 4.2.8.

Table 7.4. Transverse displacement at tip for various models (in meters)

Model	w at tip	normalized w.r.t. the plane stress model
Bernoulli-Euler	-0.01911	0.99012
Timoshenko	-0.01926	0.99786
Plane stress	-0.01930	1.00000
FE plane stress (1x10)	-0.01915	0.99195
FE plane stress (2x20)	-0.01921	0.99497
FE plane stress (4x40)	-0.01922	0.99583
FE plane stress (8x80)	-0.01923	0.99620
FE plane stress (64x640)	-0.01924	0.99690

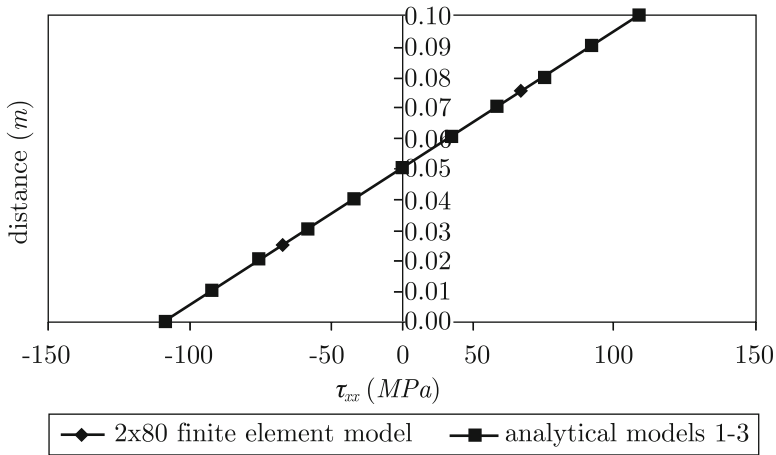


Fig. 7.9. Normal stress predictions at mid-span

However, the normal stress predictions at the built-in end shows some deviation from the solutions of models 1 to 3 and the shear stress predictions is completely different.

We report in Figures 7.13 to 7.16 the analogous results obtained with the 8×80 element model. The same trend as observed for the 2×20 element model can be seen. Now, however, the mid-span stress predictions agree very well with those of models 1 to 3 and the difference in predictions for the stresses at the built-in end are even more pronounced. If we denote by A the top point at the built-in section, *i.e.*, $(x = 0, z = h/2)$, we note that the normal stress prediction for this point is much higher than that obtained with models 1 to 3. Regarding the shear stress at the built-in section, we note that although the shape of the shear stress curve is similar to that obtained with

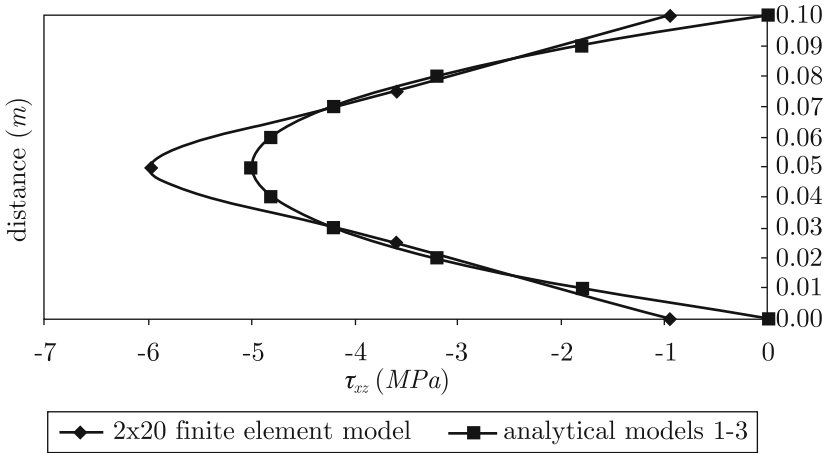


Fig. 7.10. Shear stress predictions at mid-span

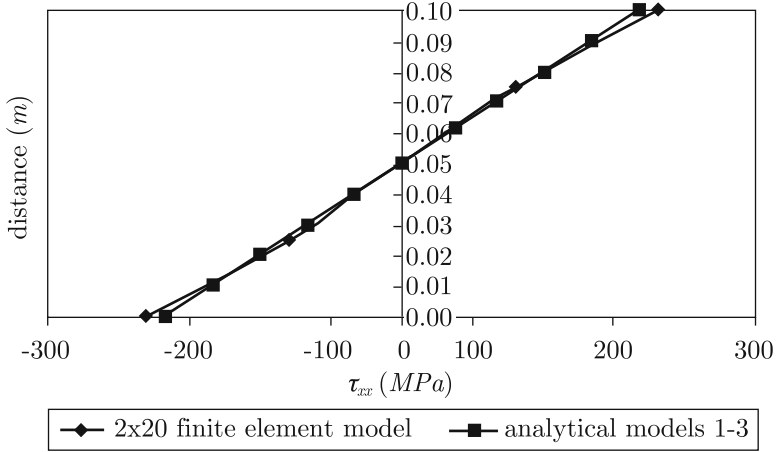


Fig. 7.11. Normal stress predictions at built-in section

the 2×20 element model, the values are substantially different, especially at point A.

The results reported indicate that as we refine the mesh the stresses increase in the vicinity of point A. In fact, for the boundary conditions described in Figure 7.3, it can be shown that the stresses which correspond to the exact solution of the mathematical model are singular at point A, *i.e.*, they tend to infinity (see Timoshenko and Goodier, 1970). Considering the hierarchical process, it is crucial to realize that this model is only one model in our hierarchical sequence and our primary objective is to arrive at good predictions for the actual physical problem at hand. Therefore it is essential at this point to use the concept of the very-comprehensive mathematical model introduced

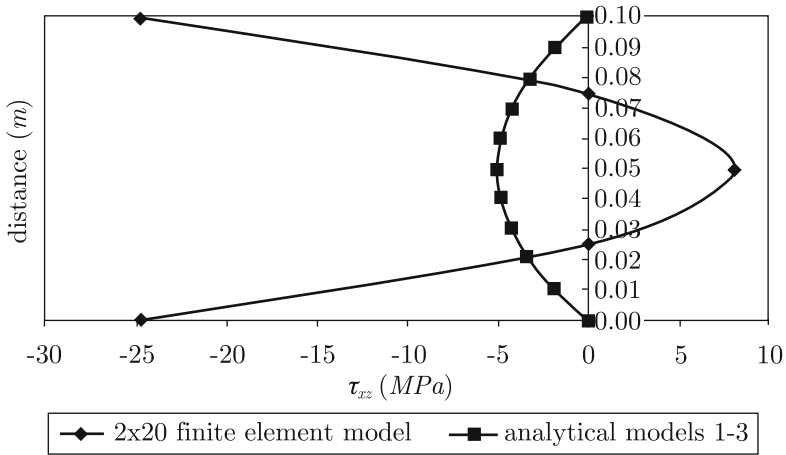


Fig. 7.12. Shear stress predictions at built-in section

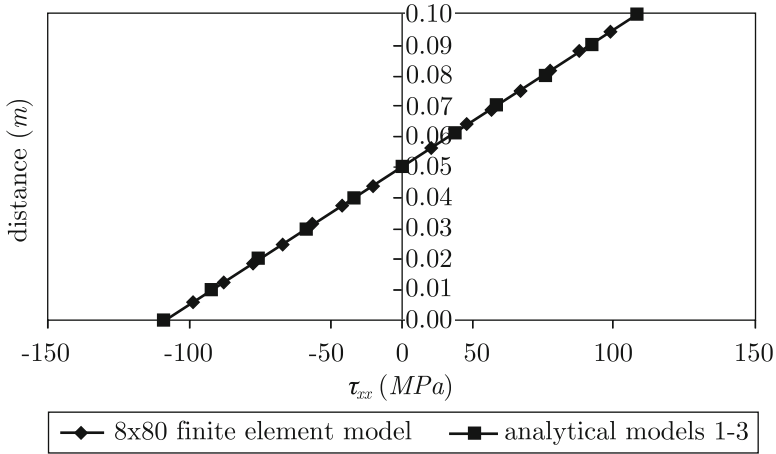


Fig. 7.13. Normal stress predictions at mid-span

in Chapter 1. Of course, in such a model the stresses would not tend to infinity as predicted by the elasticity model for the problem in Figure 7.3, since in the very-comprehensive mathematical model inelastic deformations would occur as the stresses exceed some limit values. Moreover, the sharp corner at point *A* is “not really sharp” in the physical problem and in the very-comprehensive mathematical model this fact would be represented by some geometric rounding of the corner. Another consideration that should be reflected in the very-comprehensive mathematical model is the fact that the support is “not really rigid” and the boundary conditions shown in Figure 7.3 are not really representative of what happens in the physical problem. In order to improve the model in this respect, a portion of the adjoining domain

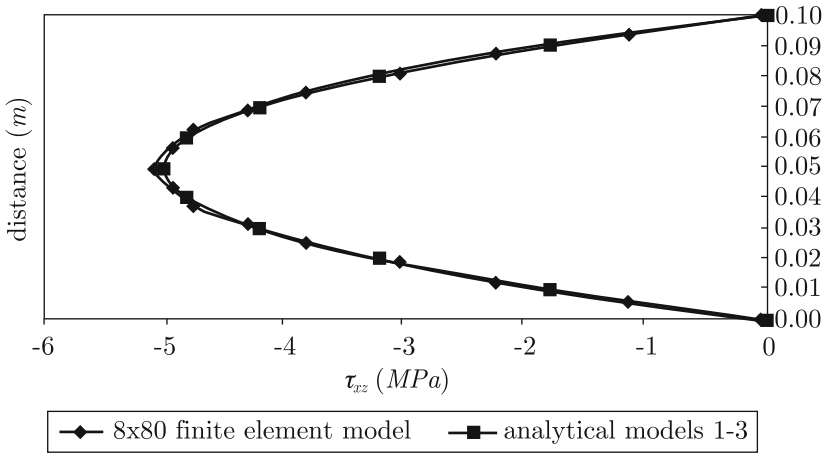


Fig. 7.14. Shear stress predictions at mid-span

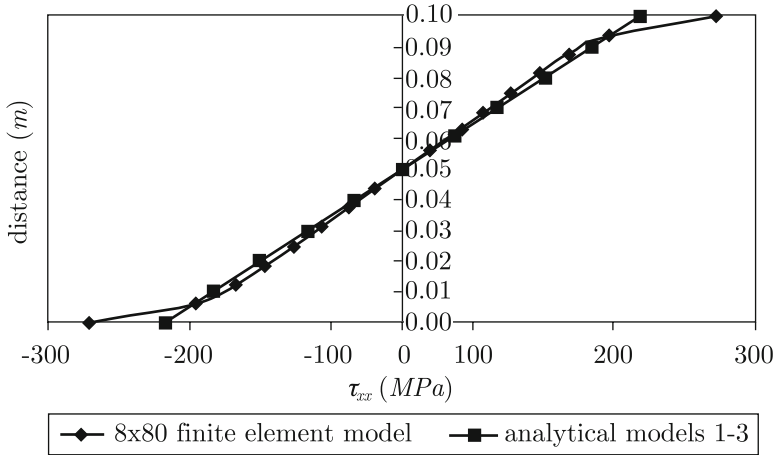


Fig. 7.15. Normal stress predictions at built-in section

at the built-in end should be included in the model representing the flexibility of the material in that region.

In light of the above discussion, we introduce two additional models in our hierarchical sequence. First we consider some rounding of the corners at the built-in end and next we model the adjoining region to the built-in end, which is made of steel. We could also introduce elasto-plastic effects. However, we choose not to do so here since nonlinear formulations are discussed only in the next chapter.

In Figure 7.17, the geometric model with the rounding is described. We note that the rounding is a very small feature and it was introduced adding material in such way that point *A*, shown in the detail of Figure 7.17, is

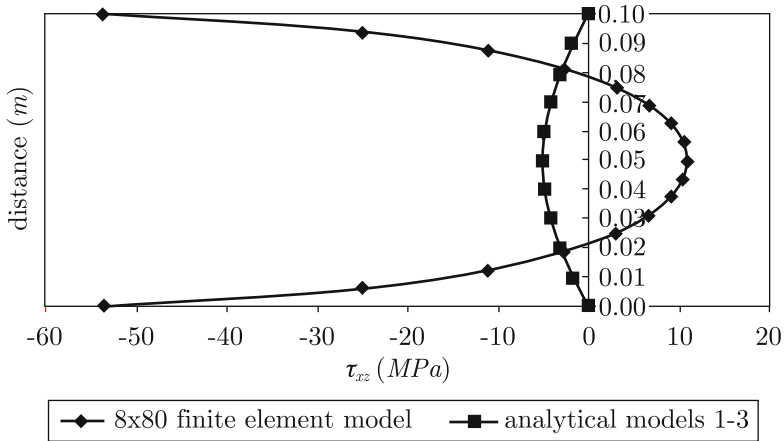


Fig. 7.16. Shear stress predictions at built-in section

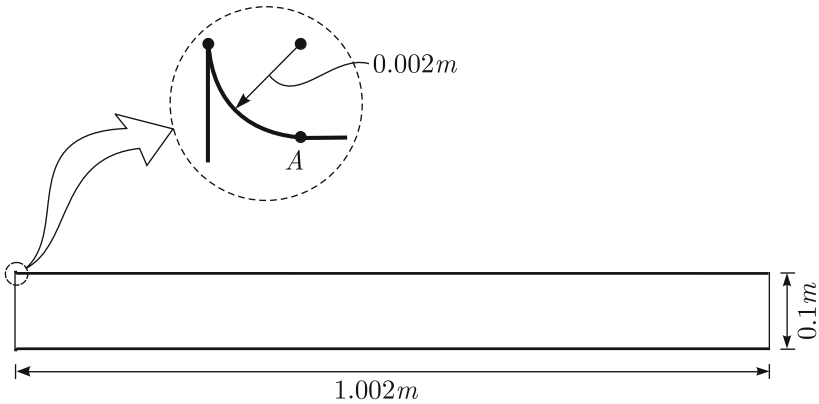


Fig. 7.17. Geometric model with the rounding

at the same geometric location as before, *i.e.*, $x = 0$, $z = h/2$. We study the stresses at the section defined by point *A* and since the stress resultants at this section are the same as those of the built-in section of the model described in Figure 7.3 comparisons are allowed. Since we expect to have removed the singularity at point *A* due to the rounding, the solution to the mathematical model should display a vanishing shear stress at point *A* due to the horizontal free edge. However, to predict this vanishing shear stress along free edge an extremely fine mesh needs to be used because of the very small radius of curvature of the feature.

In Figures 7.18 and 7.19 we report the normal and shear stress predictions respectively. We can see that the shear stress drops back to zero as point *A* is approached. In Figure 7.20, a detail of the variation of the shear stress in the vicinity of point *A* is shown. We can see the high stress gradients.

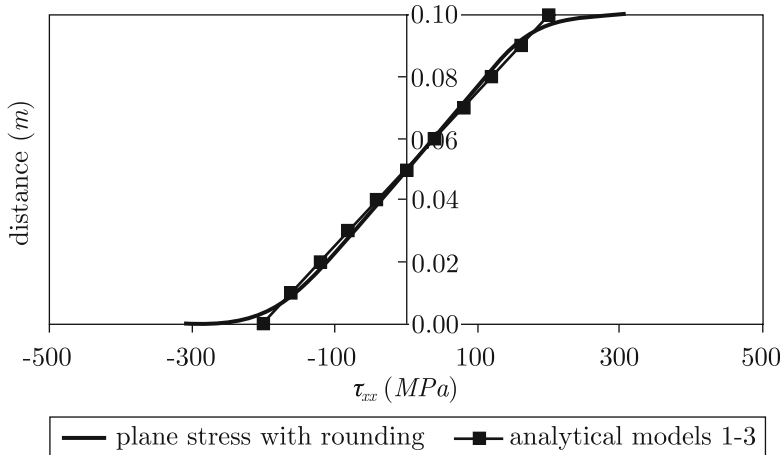


Fig. 7.18. Normal stress predictions at section that passes through point A

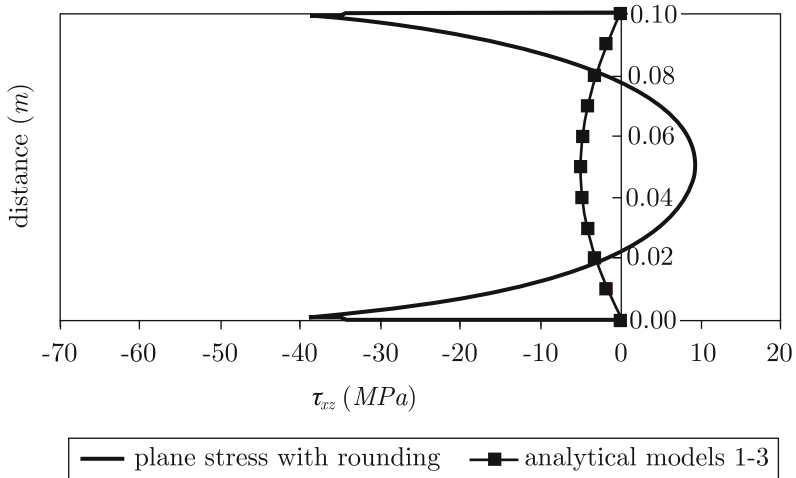


Fig. 7.19. Shear stress predictions at section that passes through point A

As a final model improvement, still in the context of linear analysis, we introduce in the model the portion made of steel. In Figure 7.21, the geometric model is summarized. We note that we have also introduced the rounding in this model. In Figures 7.22, 7.23, 7.24 we show the stress curves predicted at the section which contains point A analogous to those reported for the previous model. We see that the peak values have increased. This increase in stress may be a surprise, and is due to the fact that the aluminum material now punches into the steel support. However, the overall shapes of these curves are the same as before, retaining the qualitative behavior of the stress predictions at this section.

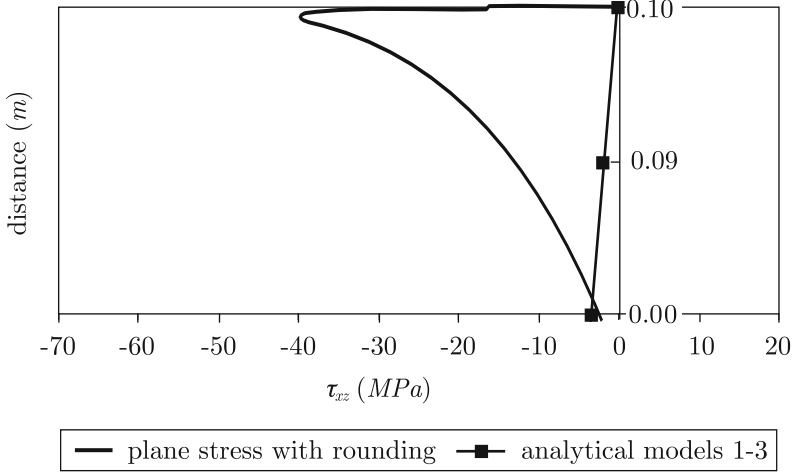


Fig. 7.20. Detail of shear stress predictions at section that passes through point *A*

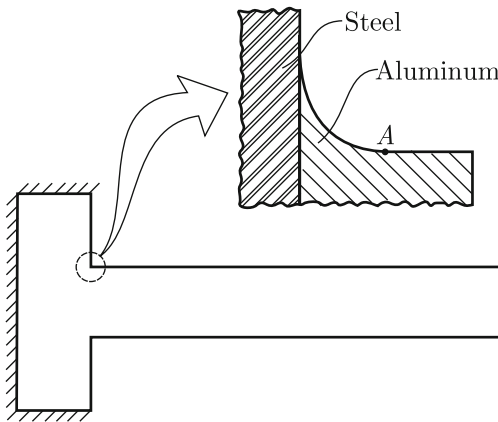


Fig. 7.21. Geometric model which includes the steel portion. Material properties of steel are $E = 210$ GPa and $\nu = 0.3$

We might say that this last model captures all the basic phenomena which can be represented in linear analysis. Of course, some improvement could still be obtained by introducing an elasto-plastic constitutive law for the materials involved. Since the yield stress of the aluminum considered is $\tau_y = 223$ MPa we expect a decrease in the stress prediction near the vicinity of point *A*. Nevertheless, such modifications should not qualitatively change the distribution of the stresses at the section which contains point *A*. Therefore, the stress distributions shown in Figures 7.22 to 7.24 should be relatively close to those of the very-comprehensive mathematical model. Note that the shear stress distribution at the section which contains point *A* is qualitatively

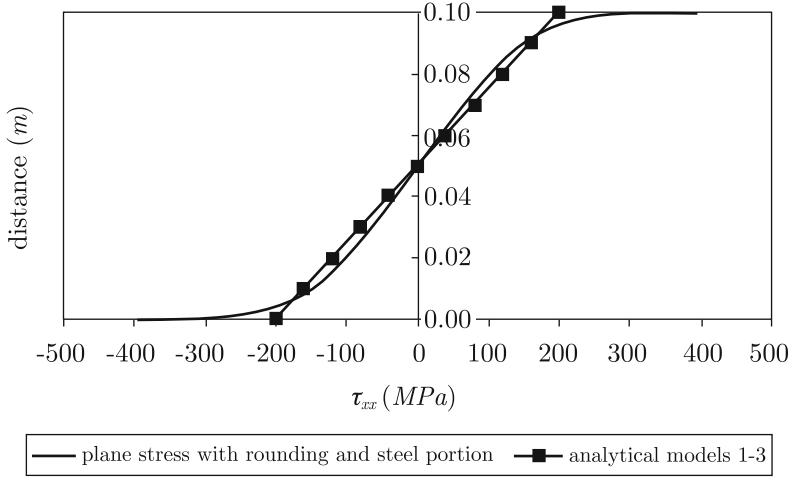


Fig. 7.22. Normal stress predictions at section that passes through point *A*

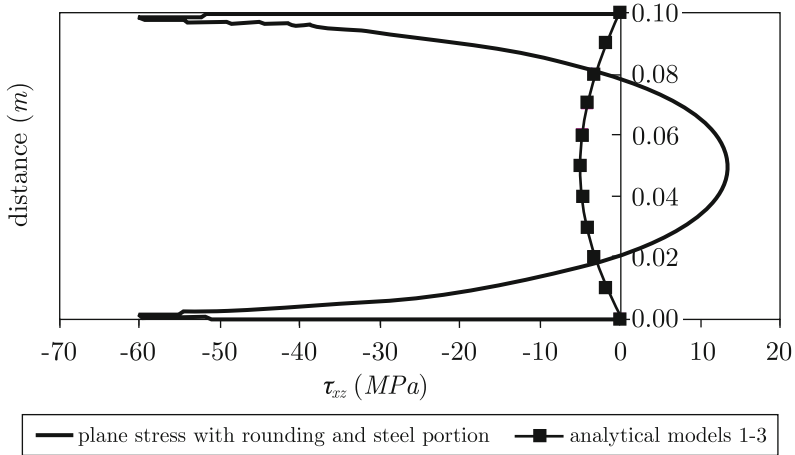


Fig. 7.23. Shear stress predictions at section that passes through point *A*

(and hence also quantitatively) completely different from the predictions of models 1 to 3 which are routinely used for such kind of analyses. This result illustrates the importance of hierarchical modeling for this case if accurate stress predictions are required for this section.

7.2 Machine Tool Jig

In Figure 7.25 the machine tool jig to be analyzed is schematically shown. We assume that the displacement boundary conditions and the loading of the

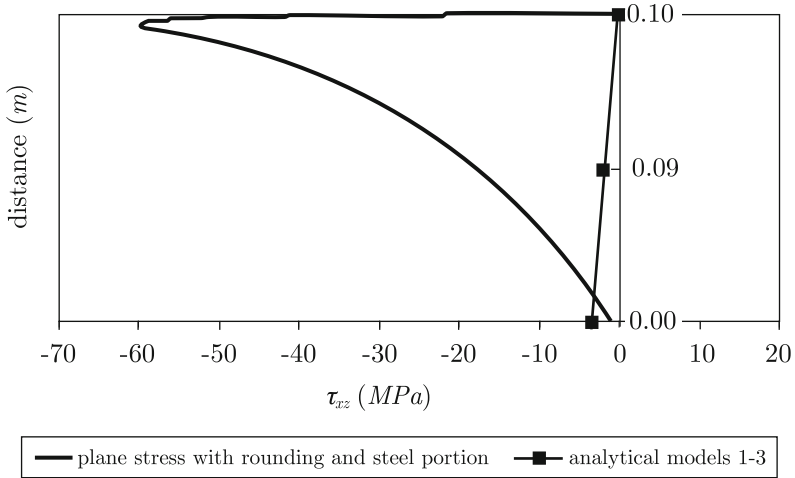


Fig. 7.24. Detail of shear stress predictions at section that passes through point A

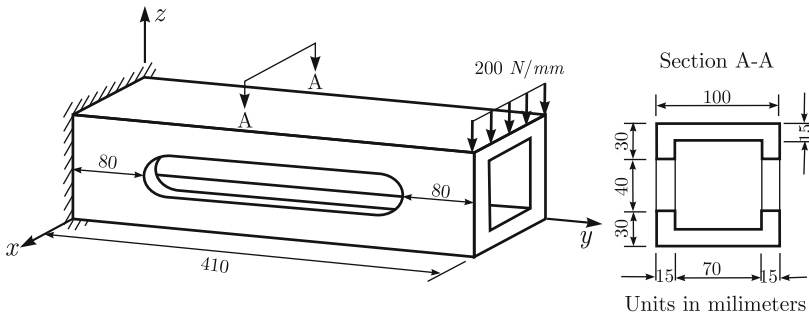


Fig. 7.25. Machine Tool Jig problem description

physical problem are accurately modeled by the idealization represented in Figure 7.25. Therefore, we concentrate on the structural modeling of this idealization.

The variables to be predicted are the transverse displacement and the stresses. These variables are chosen, since there are limit values for the transverse displacement, due to operational requirements, and for the stresses, to guarantee structural integrity.

Our objectives are to obtain a qualitative understanding of the structural behavior of the part and to investigate which models would predict the transverse displacement with a precision of around 15 % and the stresses within a margin of 20 % error.

Our sequence of hierarchical models is:

- 1) Model 1: Beam model

- 2) Model 2: Shell model
- 3) Model 3: Three-dimensional elasticity model.

We detail below the models used.

7.2.1 Beam Model

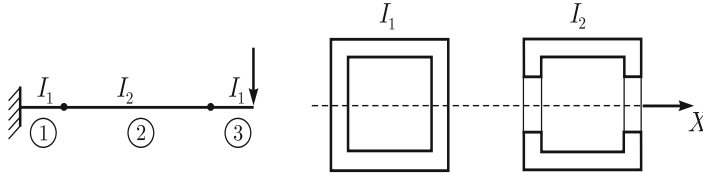


Fig. 7.26. Uniaxial beam model, in each case the moment of inertia is, as in Section 4.2.2, taken about the X -axis

The simplest beam model is shown in Figure 7.26 which is obtained by considering Bernoulli-Euler beam elements with different cross-sections. This model is included here with the only purpose of showing, in a very simple context, an example of bad modeling. The mid-beam element, represented in Figure 7.26 by number 2, does not represent the basic mechanical behavior of the part in this region. The reason is that due to the presence of the side openings, there is no physical connection between the top and bottom parts of any section in this region. Therefore, these top and bottom parts do not behave as geometric subdomains of the same beam section, and the fundamental hypothesis of the Bernoulli-Euler beam theory, that beam sections remain plane (with the shear force resisted on a connected section) is violated. Some results obtained with this model are shown later to give an idea of how far off these solutions may be when compared to solutions obtained with properly selected models.

The beam model described in Figure 7.27 should be able to capture the qualitative behavior of the part. In this model, the top and bottom parts of the tool in the opening region are modeled with separate beams, represented by elements 3 and 4, with sections shown also in Figure 7.27. The rigid links as discussed in Section 6.6.3 can be understood as constraints which enforce that the rotations of nodes 1, 3 and 5 should be the same as well as those of nodes 2, 4 and 6. This modeling assumption is justified since the parts of the model which have a box type section, represented by elements 1 and 2, do behave approximately as beam sections having moment of inertia I_1 . Note that these beam elements with box type section are quite rigid when compared to the beam elements of the open region. Therefore, it is a consistent modeling hypothesis to assume that, at the geometric section where elements 3 and 4 meet with element 1 at the left side, and with element 2 at the right side,

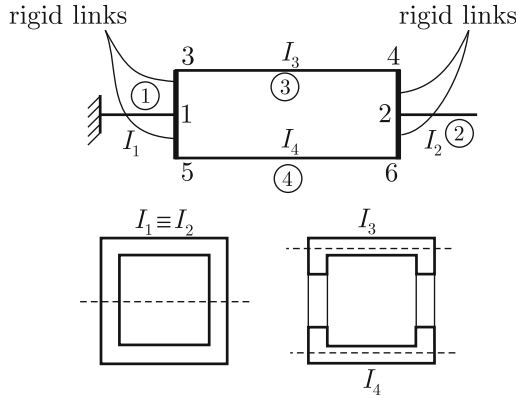


Fig. 7.27. Beam model with rigid links

the rotations are the same since the box type sections remain plane during deformations.

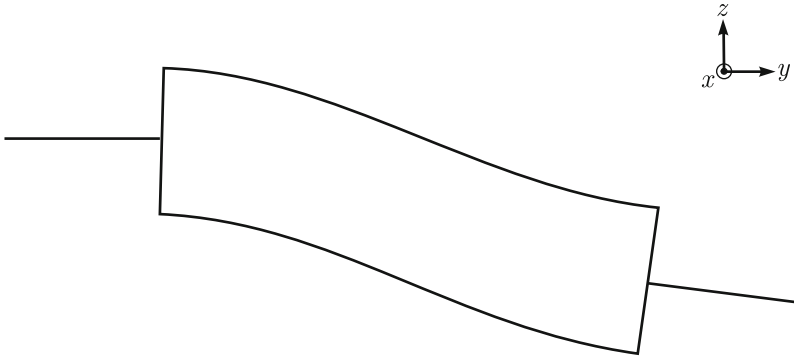


Fig. 7.28. Magnified deformed configuration of beam model with rigid links

To obtain more insight into the behavior of this model we show in Figure 7.28 a magnified deformed configuration representing only the bar axes. We can easily recognize that most of the deformation occurs in the central part of the model which behaves as a frame that is being sheared and subjected to an external moment. In Figure 7.29 the bending moment and axial force diagrams are shown confirming this frame type behavior. It is interesting to contrast the behavior of this beam model with that described in Figure 7.26 which is deemed to represent a “bad” modeling. For this purpose, we select a section of the model as shown in Figure 7.30 and compare qualitatively the internal forces and stresses. The distribution of normal stresses shows totally different predictions. While in the model presented in Figure 7.30b, the

top and bottom parts bend individually, the model of Figure 7.30a predicts that the section bends as a whole. Consequently, the stress distributions, schematically shown in Figure 7.30 for section $B - B$, reflect these distinct behaviors leading to totally different predictions.

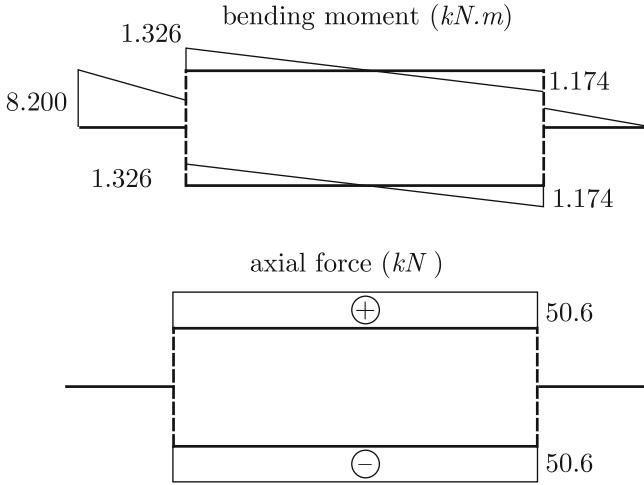


Fig. 7.29. Bending moment and normal force diagrams for beam model with rigid links

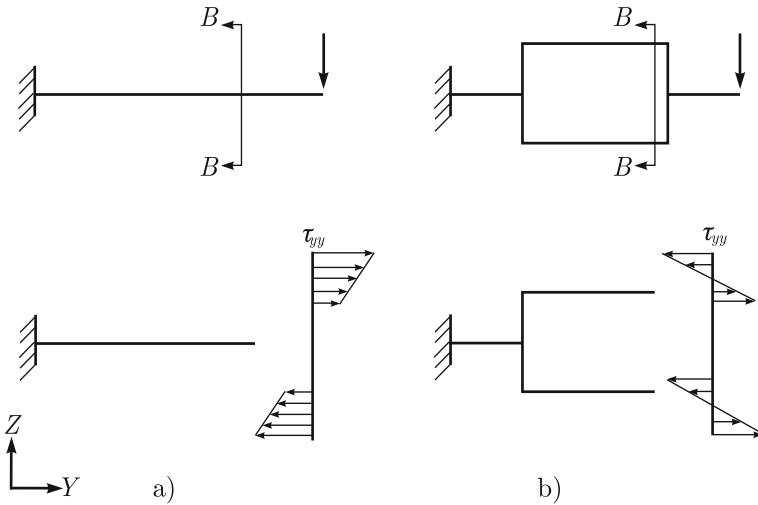


Fig. 7.30. Schematic longitudinal normal stress distributions for beam models. a) Model of Figure 7.26; b) Model of Figure 7.27

7.2.2 The Shell Model

This model represents the part as a shell structure. We note that the thickness/length ratio of this shell model is given by $15/100 = 15\%$ if we take the width to be the representative length size. Therefore, if the behavior is to be represented by a shell structure, we need to consider at least a moderately thick shell model. Even using such a model, if we look at the corners of the open regions, as indicated in Figure 7.31, and consider the actual dimensions of the problem, we might expect the behavior to be mostly three-dimensional in these regions. This fact partially justifies the use of model 3 of the sequence. Nevertheless, the shell model should provide a better description of the behavior of the open regions (the rounded part) than the beam model and predict spatial variations of the variables along the width direction which are, of course, not predicted by the beam model.

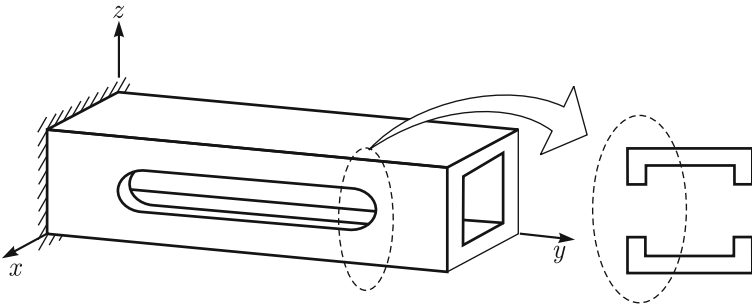


Fig. 7.31. Detail near end of open region

The solution of the shell model is obtained in a finite element analysis. The elements used are solving the (mathematical) basic shell model (see Section 4.4.2) and, therefore, the predictions include the effects of shear deformations. A sufficiently fine mesh, shown in Figure 7.32, of eight-node elements is used to ensure that the solution obtained is close to the solution of the mathematical model. We present the results of this analysis in Sections 7.2.4 and 7.2.5.

7.2.3 Three-Dimensional Elasticity Model

A motivation for the use of this model was already given when presenting the shell model, *i.e.*, the structural behavior of the part is, *e.g.* in the corner regions, of a three-dimensional nature due to the geometric and loading conditions. Therefore, an enhancement in predicted behavior is expected when considering a three-dimensional model. Again, a sufficiently fine mesh, now of twenty-node hexahedral elements, is considered as shown in Figure 7.33.

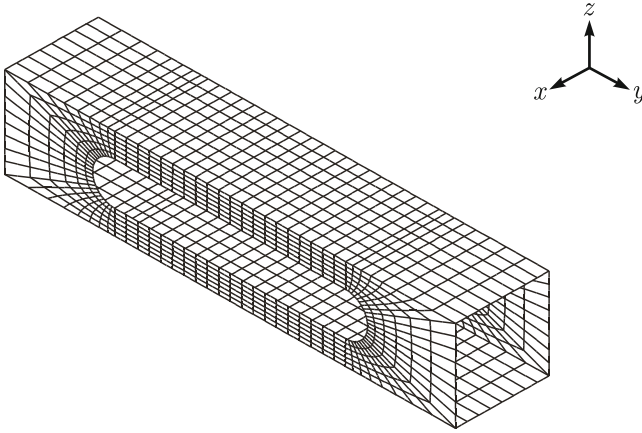


Fig. 7.32. Finite element mesh for the shell model

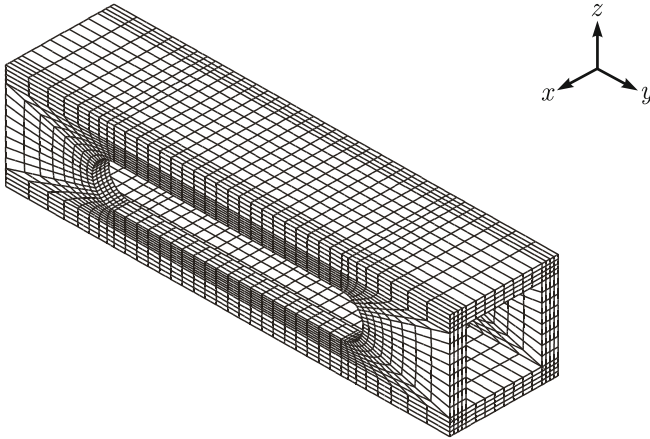


Fig. 7.33. Finite element mesh for 3-D model

A magnified deformed configuration of the 3-D model is shown in Figure 7.34. We observe that the gross behavior is consistent with that of the beam model with rigid links.

7.2.4 Qualitative Analysis

The qualitative behavior of the displacements was, to some extent, already examined. Both end parts are very rigid and behave as box sections. The central part – the open region – has a frame type behavior in shear and the top and bottom parts behave as beams.

In Figure 7.35, we select some lines of the part to examine the predicted results. In Figure 7.36, we show the transverse displacement, *i.e.*, the dis-

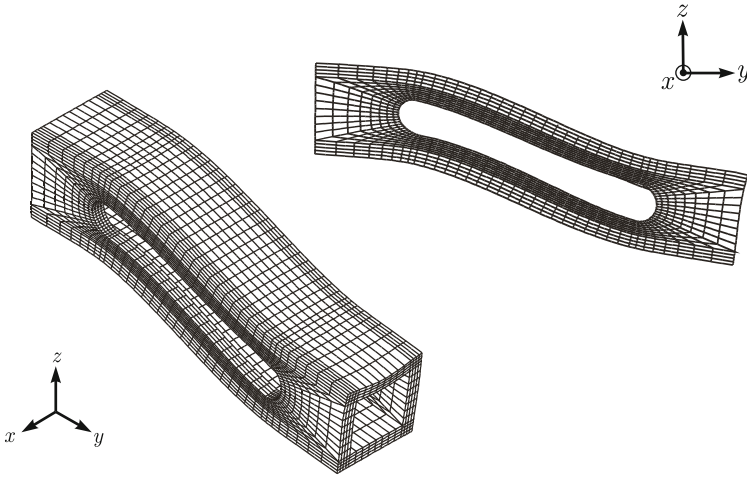


Fig. 7.34. Magnified deformed configuration for the 3-D model

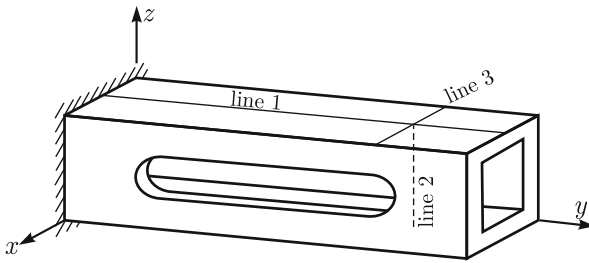


Fig. 7.35. Selected model lines

placement in the z -direction, along line 1. We note that the gross behavior is captured by the three valid models. Naturally, the beam model with rigid links is the most stiff while the 3-D model is the least stiff. As might be expected, or may be a surprise if Figure 7.30 has not been studied, the beam model of Figure 7.26 does not capture the behavior at all, being much too stiff. In Figure 7.37 we show the stress τ_{yy} , which is the normal stress associated with bending, along line 1. We note that in the central open region $120 < y < 270$ the three valid models lead to quite close predictions. However, the behavior is complex and the peak stresses are not well predicted by the beam model with rigid links. We also include the results obtained with the beam model of Figure 7.26. As now expected considering Figure 7.36, this model completely misses the behavior of the tool jig with respect to stresses.

The stresses along line 2 are shown in Figure 7.38. This figure reveals that the qualitative behavior of the top and bottom parts is predicted by

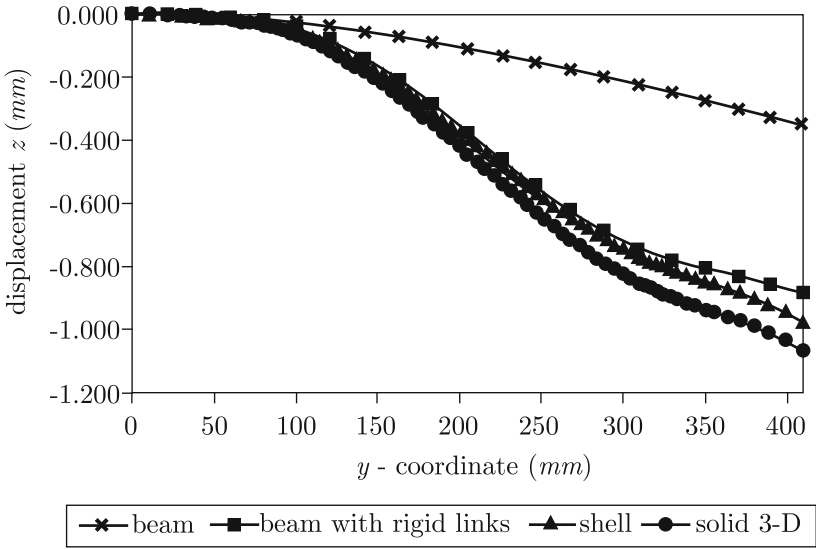


Fig. 7.36. Transverse displacement along line 1

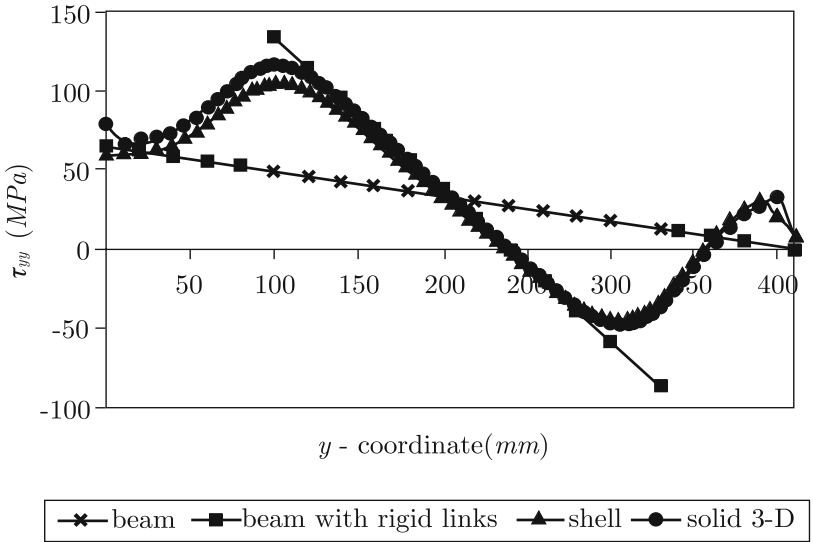


Fig. 7.37. Longitudinal normal stress along line 1

all models except by the beam model of Figure 7.26 which leads to wrong predictions.

The results along line 3 are reported in Figure 7.39. Of course the beam models predict constant stress values along this line. The 3-D and shell models can predict the variation along the width. We point out that the results

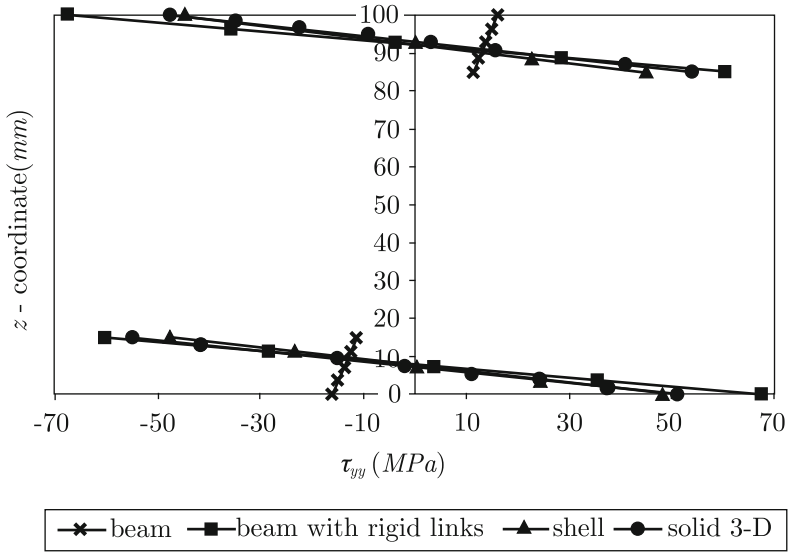


Fig. 7.38. Longitudinal normal stress along line 2

Table 7.5. Transverse displacement at selected points (in mm)

Model	P1	P2	P3
Beam	-0.355	-0.227	-0.110
Beam with rigid links	-0.884	-0.747	-0.375
Shell	-0.976	-0.772	-0.400
Solid 3-D	-1.067	-0.853	-0.442

reported for the shell model do not extend to the lateral faces of the part, since, at the corner, the shell node is located at the midsurface implying that the geometric domain in the corner region is not fully represented in the shell model.

7.2.5 Quantitative Analysis

We do not perform a comprehensive quantitative analysis. Our purpose is to only show the numerical results at some selected points, defined in Figure 7.40, to obtain an estimate of the accuracy of the results.

In Table 7.5 we report the transverse displacement results and in Table 7.6 the same results are shown normalized with respect to the results of the 3-D model, our highest order model. We note that the hierarchical order of the selected models is confirmed by the displacement predictions, *i.e.*, the beam model with rigid links displays an “error” of around 15% and the shell

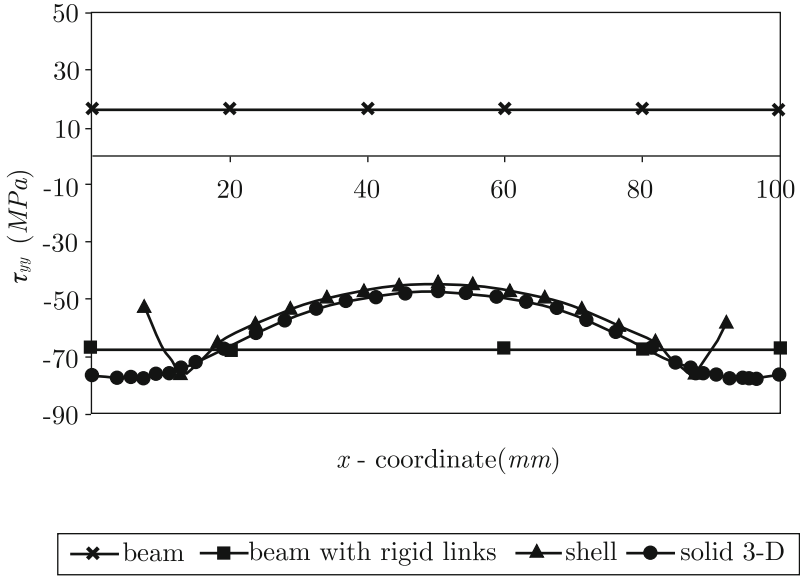


Fig. 7.39. Longitudinal normal stress along line 3

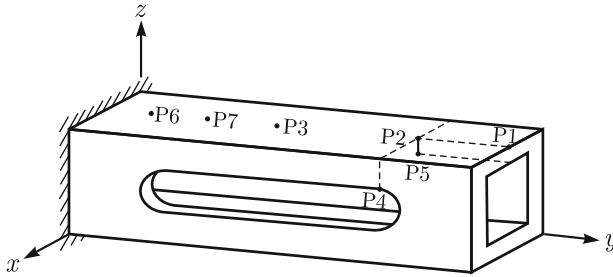


Fig. 7.40. Selected model points

model an error of about 10% when compared with the 3-D model results.

Table 7.6. Normalized transverse displacement at selected points

Model	P1	P2	P3
Beam	0.333	0.266	0.249
Beam with rigid links	0.828	0.876	0.848
Shell	0.915	0.905	0.905
Solid 3-D	1.000	1.000	1.000

Table 7.7. Longitudinal normal stress at selected points (in MPa)

Model	P2	P4	P5	P6	P7
Beam	16.20	6.48	11.34	61.40	46.82
Beam with rigid links	-67.35	187.97	60.31	61.40	113.66
Shell	-44.48	190.76	45.02	61.37	99.52
Solid 3-D	-47.54	206.12	53.94	69.19	108.98

Table 7.8. Normalized longitudinal normal stress at selected points

Model	P2	P4	P5	P6	P7
Beam	-0.341	0.031	0.210	0.887	0.430
Beam with rigid links	1.417	0.912	1.118	0.887	1.043
Shell	0.936	0.925	0.835	0.887	0.913
Solid 3-D	1.000	1.000	1.000	1.000	1.000

The uniaxial beam model of Figure 7.26, due to the wrong representation of the kinematics, is much too stiff.

In Table 7.7 we show the stress τ_{yy} at selected points and in Table 7.8 the same predictions are reported normalized with respect to the 3-D model.

The analysis of the results for the stresses is more intricate, since the quality of the predictions for the same model may significantly vary from region to region. For example, point P7 falls in the central region for which the beam model with rigid links captures the behavior of the structure quite well, leading to a quite accurate prediction. As discussed earlier, points P2, P4 and P5 are located in a region of complex behavior for which we should not expect accurate predictions from the beam model with rigid links. In fact, the point P2 prediction by this model is off by around 40% with respect to the 3-D model. We note that this result is also seen in Figure 7.39, and is due to the variation of the stress along the width direction.

Of course, the structure being analyzed is statically determinate. Therefore, the resultant forces that are transmitted by any section are the same for all models considered. This is the reason why the stress prediction for point P6 is relatively accurate even for the uniaxial beam model: since at the section of point P6 the structure behaves as a beam with a box section, and since the stress resultants are exactly predicted we obtain reasonable predictions for the stresses. The situation would be quite different if the structure were supported at a point (e.g. $y = 410$) preventing the transverse displacement at this point. In such a case, the structure would be statically indeterminate and the accuracy of the resultant forces would depend on the accuracy of the displacement predictions as well.

We can summarize the conclusions regarding the analysis of the structural idealization of Figure 7.25 as follows:

- The beam model with rigid links, the shell and 3-D models capture the qualitative behavior of the structure for displacements and stresses. The uniaxial beam model fails to represent the behavior in the open region and should not be used.
- The beam model with rigid links, being the simplest model that properly captures the behavior, could be used to understand the behavior of the structure when performing parametric studies involving variations of the geometric characteristics.
- Only the shell and 3-D models gave predictions that have the required accuracy (15% for displacements and 20% for stresses). Here it is implicitly assumed, as a modeling consideration, that the predictions of the 3-D elasticity model are very close to the predictions of the very-comprehensive model for the regions of interest. Of course, this is the case only if the loading is limited to a value which leads to stresses that are well below some limit values, namely those which would cause yielding of the material and/or lead to geometric nonlinear behavior.

7.3 Modeling of a carabiner

The modeling of the carabiner was discussed in Chapter 1 to introduce the main concepts of the hierarchical modeling process. The description of the physical problem is given in Section 1.2.1 and is not repeated here. As in Section 7.2, our objective is to calculate the displacements and stresses to an accuracy of about 15% and 20%, respectively. Referring to Figure 1.10 we consider in this section the following hierarchical models:

- 1) Model 1: Straight bar model
- 2) Model 2: Curved bar model
- 3) Model 3: Three-dimensional elasticity model.

7.3.1 Straight bar model

The model is constructed using straight Bernoulli-Euler beam elements. The end-points of each beam element are placed on the axis of the geometric model of the carabiner. An elliptical cross-section is chosen to describe the part. In Figure 7.41 we show the model where the diamond symbols indicate the end-points of the elements. We see that in the curved regions many elements were chosen to properly describe the geometry.

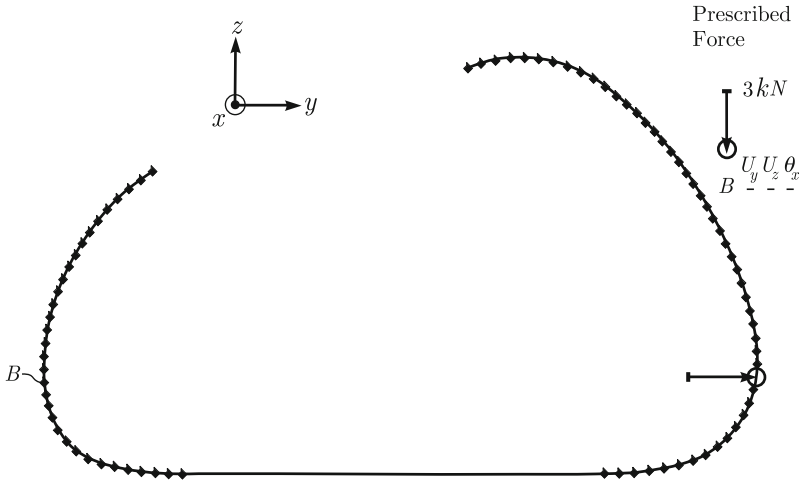


Fig. 7.41. Finite element mesh for beam models. The material of the carabiner is aluminum with $E = 70 \text{ GPa}$, $\nu = 0.33$

7.3.2 Curved bar model

For this model we use general curved 3-node beam elements (See Section 6.4.4). We recall that in this beam element formulation the geometry of the element is interpolated from the cross-sections at the nodes, and therefore the mesh represents, in an approximate manner, the curved geometry. The discretization used is defined by the nodal positions shown in Figure 7.41, *i.e.*, both beam models have the same nodes but, of course, not the same elements since in this model we have 3-node elements. Note that these curved beam elements can model thick beams and include the effect of shear deformations.

7.3.3 Three-dimensional elasticity model

The three-dimensional finite element model is constructed from the solid model shown in Figure 7.42a. We note that this solid model has a number of features such as the hole for the pin and letter imprints, which, if considered in the finite element model, would render the model very large, adding little relevant information for the structural behavior of the part. Therefore, a defeaturing of the geometric model was undertaken leading to the geometry shown in Figure 7.42b (see Section 6.8). We note that the geometric model shown in Figure 7.42b was constructed for the finite element discretization procedure, *i.e.*, only half of the geometry is considered due to symmetry conditions and surfaces are conveniently created for the application of the boundary conditions which are directly imposed on the geometric model, as shown in Figure 7.43. An automatically generated and sufficiently fine mesh is displayed in Figure 7.44. We use this mesh, instead of the mesh in Figure 6.84, because such tetrahedral element meshes are typically used in practice.

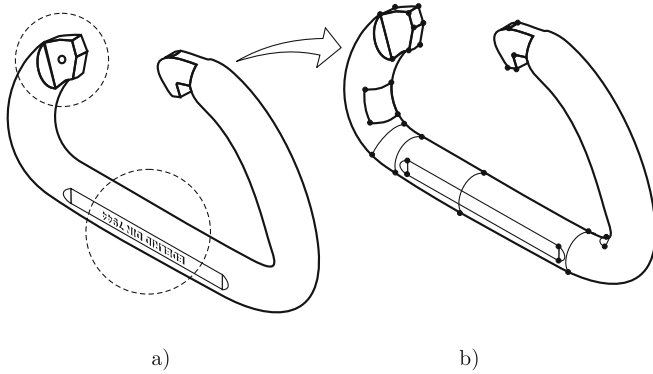


Fig. 7.42. Defeaturing process

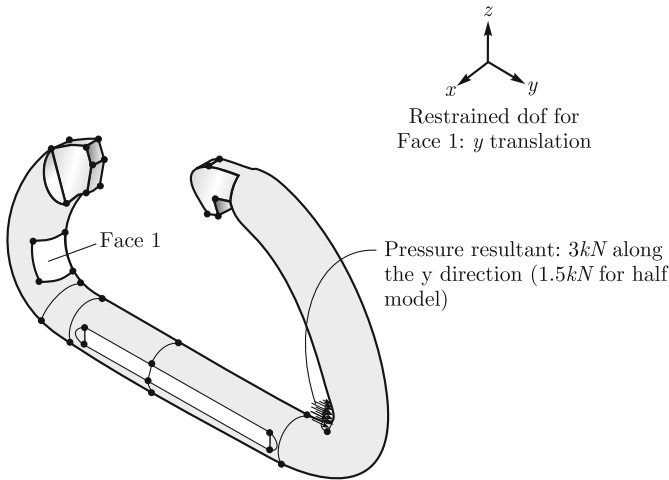


Fig. 7.43. Geometric model prepared for finite element mesh construction

7.3.4 Qualitative analysis

The qualitative behavior of this structural part is very simple and it should be captured by all models. Both, displacements and stresses are mainly due to bending actions. In order to obtain insight into this behavior, let us refer to Figure 7.45 where we schematically show the moment diagram that we should expect for a bar representation of the part. Due to the statically determinate nature of the problem, the moment distribution is that reported in Figure 7.45 for all models considered. Hence, the induced displacement and stress patterns should be qualitatively similar to each other for the models studied since they are primarily due to bending. In other words, for a given section, the bending moment, which is equal for all models, is transferred by normal stresses. However, considering the bending moment stresses

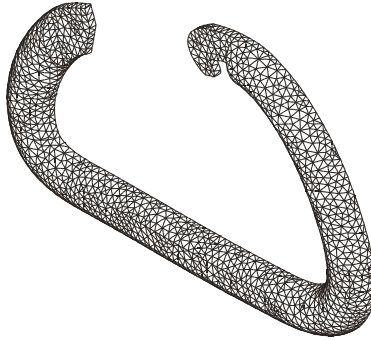


Fig. 7.44. Finite element mesh for 3-D model

more closely, in the regions where the geometric axis of the part is straight we expect a linear stress distribution through the thickness for all models. But in the regions where the axis is curved we *only* have a linear normal stress distribution for the Bernoulli-Euler beam model, since each element is straight, and that distribution irrespective of how many straight elements are used to represent a curved region. Hence a surprise may be that convergence to the stresses of a strongly curved thick beam can never be reached with this model. Considering the other two models, the normal stress distribution will deviate significantly from linearity. For curved bar models in which the height of the beam section is large when compared with the radius of curvature of the axis, the normal stress distribution is hyperbolic (see Section 4.2.7). Therefore, significant differences in predictions are primarily expected in the curved regions of the structure, and for the peak normal stress.

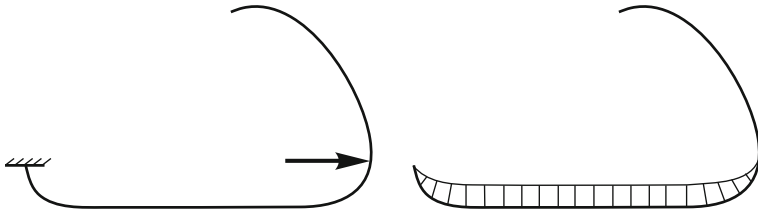


Fig. 7.45. Schematic bending moment diagram

7.3.5 Quantitative analysis

In Figure 7.46 we show some selected points for which numerical predictions are reported below. In Table 7.9 the displacements in the Y direction for points P_1 and P_2 are shown. The values are normalized with respect to

Table 7.9. Displacement in the y direction at selected points

Model	Displacement y (mm)		Normalized displacement y	
	P1	P2	P1	P2
Straight bar	2.976	0.967	0.921	0.949
Curved bar	2.952	0.971	0.914	0.953
3-D solid	3.230	1.019	1.000	1.000

Table 7.10. Displacement in the z direction at selected points

Model	Displacement z (mm)			Normalized displacement z		
	P1	P2	P3	P1	P2	P3
Straight bar	-0.881	-2.530	-1.712	0.936	0.912	0.926
Curved bar	-0.900	-2.527	-1.704	0.956	0.911	0.922
3-D solid	-0.941	-2.775	-1.848	1.000	1.000	1.000

the 3-D model. The same kind of results are reported in Table 7.10 for the displacements in the z direction for points P_1 , P_2 and P_3 .

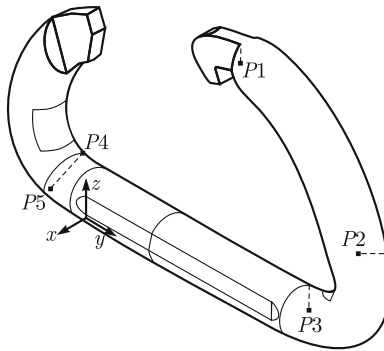


Fig. 7.46. Selected model points

Considering that the displacements at P_1 , P_2 and P_3 are representative of the overall displacement pattern of the part, we might say that the three models give relatively close displacement predictions. We can see that the beam models give very close predictions which differ, at most, by about 2%. The 3-D model gives, as expected, a more flexible behavior. The difference in prediction when compared to the beam models is relatively small falling in the range of 10%. Hence both beam models, reported upon in the tables, give results within the desired margin of error.

Let us examine the normal stress predictions for points P_4 and P_5 which are extreme points of a section in a curved region. These results are reported in Table 7.11. We see that the predictions obtained with the straight beam

Table 7.11. Normal stresses at selected points

Model	Normal stress (MPa)		Normalized normal stress	
	P4	P5	P4	P5
Straight bar	230.75	-181.30	0.569	1.417
Curved bar	402.78	-105.29	0.992	0.823
3-D solid	405.86	-127.91	1.000	1.000

model are quite far from those obtained with the 3-D model. In order to obtain insight into the normal stress behavior, we show in Figure 7.47 the normal stress distribution due to the bending moment only obtained for a straight and a curved bar model for the section in which points P_4 and P_5 are located. Of course, for the curved bar model, the radius of curvature is an important variable which for this part is given by $R = 9.85$ mm with the ratio of the section height to the radius $h/R = 1.254$. Note that the differences in predictions are significant and that the same trend as observed in the numerical predictions for points P_4 and P_5 is displayed in the results reported in Figure 7.47.

It is interesting to verify, as anticipated, that as the radius of curvature is increased the differences in predictions between the straight and curved bar models should become smaller. Indeed, the results shown in Figure 7.48 confirm this anticipated behavior.

Overall we see that the curved bar model gives a much better stress prediction, measured on the 3-D solid model results, than the straight bar model, and the stresses are almost within the desired margin of error. But for this very large ratio of h/R a 3-D solid model is more appropriate if the stresses need to be predicted very accurately.

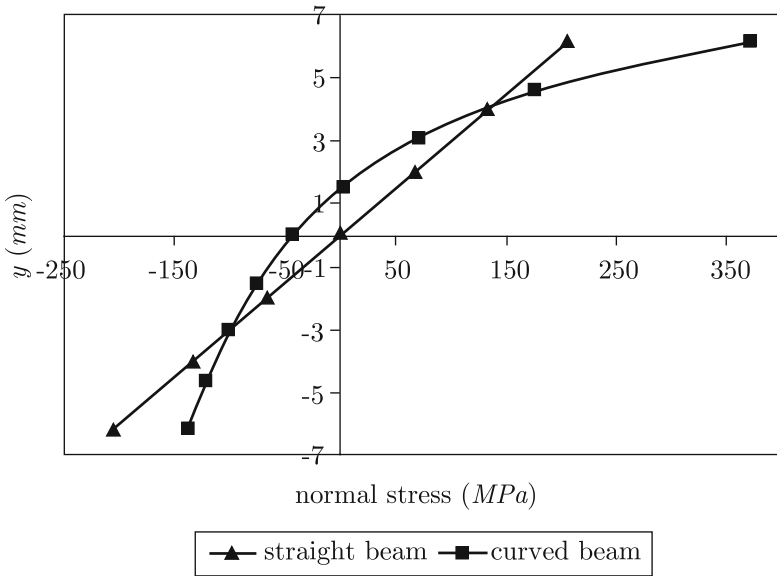


Fig. 7.47. Comparison of normal stress predictions for straight and curved beam models. For the curved model the radius of curvature is $R = 9.85 \text{ mm}$ and the section height is $h = 12.35 \text{ mm}$. The moment is 37 kNm

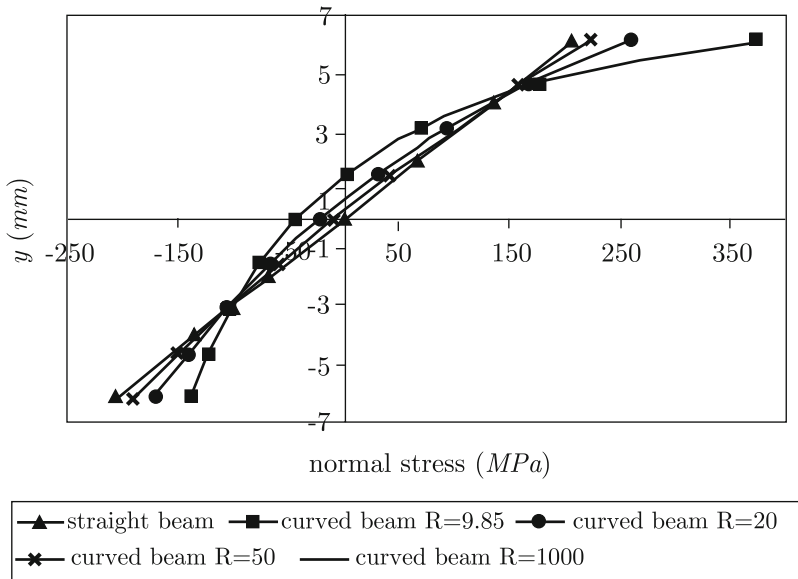


Fig. 7.48. Normal stress distribution for various radii of curvature; the $R = 1000$ results are practically equal to the straight beam results